npj | flexible electronics

Article

Published in partnership with Nanjing Tech University

https://doi.org/10.1038/s41528-025-00486-5

All-textile, chip-less, battery-free body sensor networks enabled by a concentric multi-node hub antenna architecture

Junyeong Lee[1], Mugeun Lee[1], Jinho Kim[1], Hwajoong Kim[1], Jongbin Yu[2], Namjung Kim[2] & Jaehong Lee[1] ✉

Textile-based, chip-less, wireless body sensor networks (WBANs) offer continuous, wireless monitoring of physiological signals from passive sensors distributed across body locations, representing a promising solution for daily wearable sensing. Here, we introduce an all-textile, chip-less, and battery-free textile-based body sensor network (tBSN) capable of simultaneously monitoring multiple passive sensors across the body. The tBSN is seamlessly integrated into conventional textiles via digital embroidery of flexible conductive fiber electrodes. Single-node tBSN exhibits robust wireless transmission over interconnect up to 40 cm and demonstrates durability under various conditions. By arranging multiple single-node sensor networks into a concentric multi-hub antenna architecture, we extend the system to a multi-node tBSN, enabling simultaneous wireless monitoring of distributed passive sensors within a single frequency scan. A wearable garment incorporating the multi-node tBSN tracked biomechanical signals from the vastus lateralis and knee joint during motion, highlighting its significant potential for personalized rehabilitation, fitness-assistive technologies, and advanced gait analysis.

As the global population ages and healthcare demands rise, the need for continuous monitoring of physiological parameters becomes more urgent to enable early diagnosis, effective health management, and personalized care[1–6]. Recent advances in soft wearable sensors that utilize flexible or stretchable materials allow real-time measurement of various parameters such as motion, pressure, and vital signs during everyday activities[7–12]. Because these sensors can be securely positioned on different parts of the body, they offer consistent data collection even under rigorous movement conditions, making them highly suitable for personalized rehabilitation, athletic training, and long-term health monitoring[13–15]. However, to fully exploit the potential of wearable sensors for continuous tracking and analysis, robust and user-friendly communication solutions are needed to integrate data streams from multiple sensing nodes without compromising user comfort or mobility.

Wireless Body Area Networks (WBANs) have therefore emerged as a promising solution, enabling seamless collection and integration of physiological data from sensors placed on the body[16–19]. Generally, WBANs can be classified into chip-based and chip-less categories. Chip-based WBANs typically employ well-established protocols such as Bluetooth, Wi-Fi, Radio Frequency Identification (RFID), and Near-Field Communication (NFC) to gather physiological data from sensor tags[20–27]. While recent advances in chip-based WBANs have significantly improved system flexibility and read range, these platforms still incorporate silicon-based integrated circuits that are inherently rigid[28–30]. Although such components can be mounted on flexible substrates, the overall deformability remains limited when compared to systems composed entirely of soft materials. To address these limitations, chip-less WBANs employing inductor-capacitor (*LC*) resonator-based passive sensor tags are gaining attention[31]. In these systems, an inductor and a capacitor form an *LC* circuit that resonates at a specific resonant frequency; environmental change alters the inductance or capacitance, shifting the resonant frequency of the sensor tag in a way that can be wirelessly detected through mutual inductive coupling between the sensor tag and a reader antenna[32]. By eliminating rigid, chip-based rigid components, the chip-less WBANs become inherently lightweight, battery-free, and flexible, which is ideal for continuous, unobtrusive monitoring in a wide range of practical applications[31,33–35].

In response to the growing demand for unobtrusive, lightweight, and comfortable wearable solutions suitable for everyday use, textile-based implementations of chip-less WBANs have garnered increasing attention in the field of electronic textiles[36,37]. By integrating sensing and communication components directly into textiles and clothing, these systems offer a comfortable and practical approach for collecting physiological signals during everyday activities. Recognizing this potential, recent studies have explored chip-less WBANs implementations on conventional textiles for the readout

[1]Department of Robotics and Mechatronics Engineering, DGIST, Daegu, Republic of Korea. [2]Department of Mechanical Engineering, Gachon Unviersity (GCU), Gyeonggi-do, Republic of Korea. ✉e-mail: jaelee@dgist.ac.kr

of multiple physiological signals in daily life. Dautta et al. reported a copper-foil-based passive WBANs attached to clothing for enabling the simultaneous readout of multiple chip-less sensor signals, such as temperature, pressure, salt, and pH, from a specific single location on the body[38]. While the developed passive wireless sensor network system demonstrated its ability to simultaneously read out multiple signals from chip-less sensors located in a specific body area, it still faces challenges when acquiring data from chip-less sensors distributed across multiple body parts. Li et al. developed a smart face mask with a wireless sensor network using vertically stacked intermediate relay coils for multiplexed immunoassays, achieving real-time detection of multiple biomarkers in the mask[39]. However, despite its innovative real-time monitoring capabilities for multiple biomarkers, it has limitation in flexibility due to its vertically stacked structure, critically hindering mechanical stability against dynamic deformation in practical applications. In addition, previous textile-based chip-less WBANs largely rely on metal foil-based antenna networks attached to conventional textiles, resulting in systems that are not fully integrated into the textiles and potentially compromising mechanical stability and overall reliability in real-world scenarios. Therefore, despite these advancements in textile-based chip-less WBANs, a truly seamless textile WBANs system, fully integrated into textiles and capable of monitoring multiple body locations at once, remains a challenge.

In this study, we introduce a chip-less, battery-free, textile-based body sensor network (tBSN) based on an innovative concentric multi-hub antenna design, which can simultaneously monitor wireless responses of multiple passive sensors located across various body regions. The tBSN comprises multiple single-node textile-based sensor networks, each consisting of a hub antenna, interconnects, and local antenna, where their hub antennas are concentrically integrated into a unified central hub antenna system. The resonant properties of multi-node sensor networks in the tBSN, including resonant frequencies and Q-factors, can be simultaneously and selectively monitored through the concentric central hub antenna. Based on flexible fiber electrodes, fabricated from a composite of silver nanoparticles (AgNP) and an elastomeric matrix, the tBSN effectively maintains its electromagnetic performance under various misalignment conditions between the external reading coil and central hub antenna, 10,000 intensive bending cycles, 400 repeated cycles of external mechanical pressures, and 10 intensive washing and drying cycles. We demonstrate that the tBSN can be seamlessly integrated into everyday garments, enabling continuous wireless monitoring of multiple chip-less, passive sensors to capture knee and vastus lateralis muscle movements during gait and exercise. This approach holds significant promise as a personalized rehabilitation, fitness-monitoring, and advanced gait analysis platform.

Results and discussion

Design of textile-based body sensor network system

Figure 1a depicts a textile-based Body Sensor Network (tBSN) integrated into clothing, enabling real-time, multi-node acquisition of physiological signals from chip-less, passive sensors distributed across the body. This BSN is seamlessly incorporated into garments by embroidering flexible conductive fiber electrodes, thereby ensuring robust mechanical integrity and reliable signal monitoring during everyday activities. Each single-node textile-based sensor network comprises three essential components: a hub antenna, local antenna, and interconnects (Fig. 1b(i)). Acting as the central node, the hub antenna receives wireless signals from an external reading coil and transmits them to the local antennas, subsequently collecting the reflected signals and relaying them back to the external data management system via the reading coil. The local antennas enable wireless acquisition of sensor responses to target various types of external stimuli through magnetic coupling with corresponding sensor antennas. Interconnects provide a robust transmission pathway between the hub and local antennas, efficiently conveying sensor data from spatially distributed locations back to the hub antenna. In particular, when an external reading coil is positioned on the hub antenna, the transmitted (Tx) signals from the reading coil propagate through the hub antenna and interconnects, ultimately forming a magnetic coupling with each sensor antenna aligned to a local antenna. The reflected (Rx) signals from the local antennas, dependent on sensor-specific responses, subsequently propagate back through the network and are wirelessly acquired by the hub antenna. Importantly, the scope of this textile-based sensor network can be expanded to a complete tBSN, facilitating simultaneous monitoring of distributed chip-less sensor responses across multiple-node sensor networks. This is accomplished by integrating each network's hub antenna into a concentric central hub antenna (Fig. 1b(ii)). Figure 1c presents a schematic illustration and photographs of the tBSN, comprising three single-node textile-based passive sensor networks. The wireless responses of all sensor nodes can be collected concurrently by monitoring the reflection coefficient (S_{11}) spectra of the tBSN at the central hub antenna. The concentric configuration of the central hub antenna enables simultaneous monitoring of the unique resonant frequencies corresponding to each sensor network. Since the resonant frequency of each sensor network is governed primarily by its magnetic coupling with corresponding passive sensor system, the tBSN can continuously monitor the wireless responses of the passive sensor systems by measuring the sensor-dependent resonant frequency of each network.

Figure 1d presents a photograph of the AgNP-based flexible fiber electrodes. The fabrication of the fiber electrodes proceeds through three primary steps: (i) uniform coating of a poly(styrene-block-butadiene-styrene) (SBS) polymer layer onto a nylon fiber scaffold via a dip-coating system (Supplementary Fig. 1); (ii) absorption of a substantial amount of Ag precursor into the SBS-coated nylon fibers; and (iii) direct in-situ reduction of the absorbed Ag precursor to AgNPs within the SBS layer (Supplementary Fig. 2)[40]. The combination of dip-coating and in-situ chemical reduction processes, optimized for fiber substrates, enables large-scale production of the flexible fiber electrodes, as shown in Fig. 1d. In particular, the in-situ formation process ensures a dense and uniform incorporation of AgNPs throughout the SBS polymeric matrix on the fiber, thus forming a reliable, robust electrical pathway via the AgNPs incorporated in the fiber electrodes. Figure 1e and Supplementary Fig. 3 provide scanning electron microscopy (SEM) images and energy-dispersive X-ray spectroscopy (EDS) mapping of the fabricated AgNP-based flexible fiber electrodes, confirming the uniform incorporation of AgNPs particularly in the peripheral regions of the SBS layer in the fiber electrode with an average diameter of ~316 μm. To achieve high electrical conductivity in the AgNP-based flexible fiber electrodes, multiple in situ formation cycles were repeatedly applied to a single fiber electrode. Each repetition of the in-situ formation process allowed additional AgNPs to be incorporated into the SBS polymer matrix, thereby creating supplementary conductive pathways and further enhancing the electrode's overall conductivity[41]. After five such absorption–reduction cycles, the AgNP-based fiber electrode exhibited a notable electrical conductivity of 0.22 Ω/cm (Fig. 1f). Furthermore, the AgNP-based flexible fiber electrode could successfully maintain its electrical conductivity even after 2000 cycles of bending deformation with a bending radius of 2.734 mm (Fig. 1g and Supplementary Fig. 4), highlighting its mechanical robustness and suitability for wearable applications. The high stability of the fiber electrodes is primarily attributed to the robust interfacial contacts between AgNPs incorporated in the elastic SBS scaffold which serves to maintain conductive networks under repeated mechanical deformation.

Characterization of the single-node textile-based sensor network

To fabricate the textile-based sensor network, the AgNP-based flexible fiber electrode was efficiently patterned into the single-node sensor network configurations onto standard elastic textiles by employing a digital, computer-controlled embroidery machine (Fig. 2a and Supplementary Fig. 5). While previously reported approaches typically rely on transfer of pre-patterned antenna patterns onto textiles, the digital embroidery process directly integrates the flexible fiber electrodes into the textiles, facilitating seamless integration into everyday clothing. This seamless integration

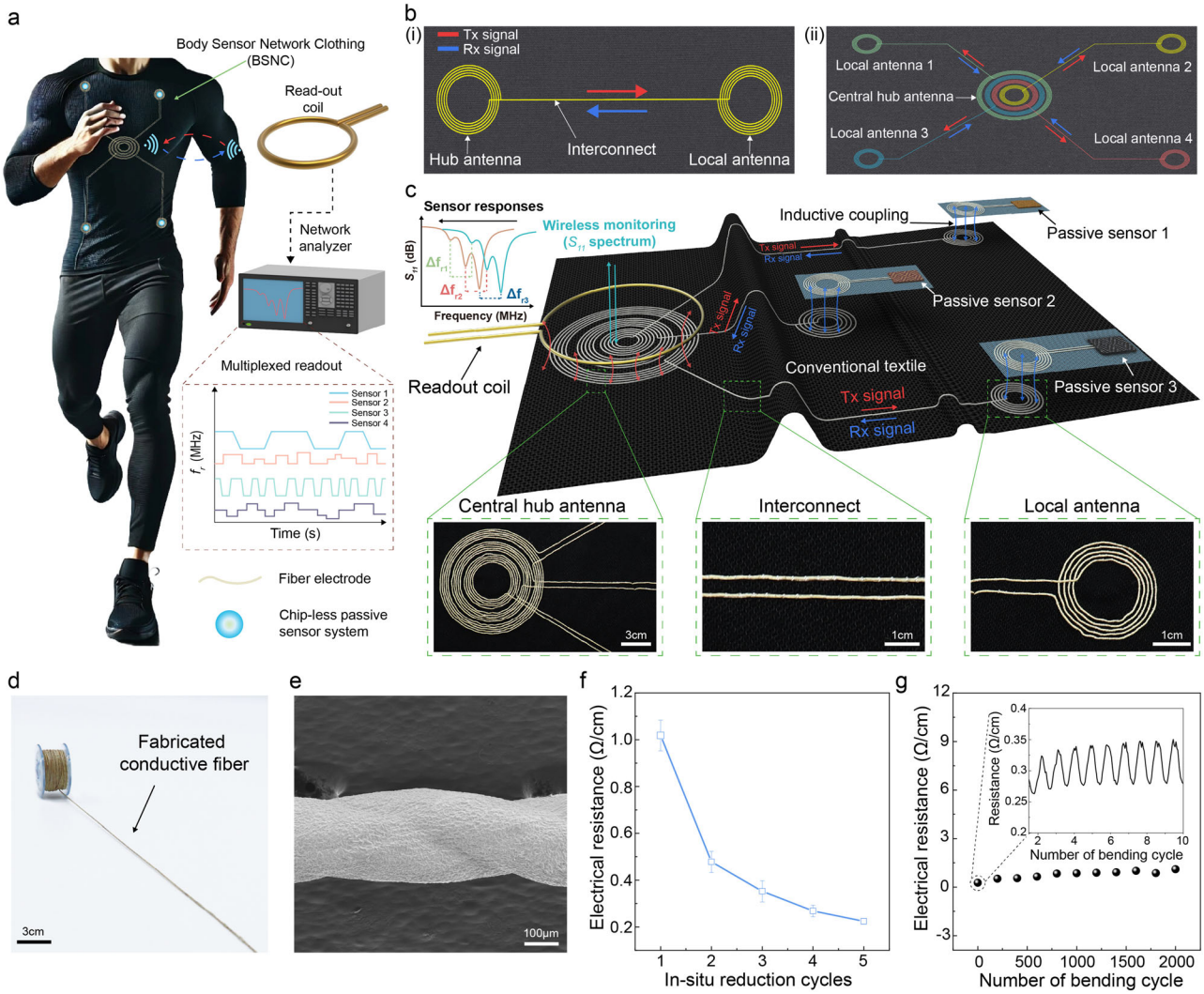

Fig. 1 | Design and fabrication of a textile-based body sensor network. a Schematic illustration of the textile-based body sensor network (tBSN) integrated into wearable clothing, enabling robust, multi-node sensing during physical activity. The system supports wireless, multiplexed readout of chip-less passive sensors via inductive coupling with an external readout coil. **b** Comparison between single-node and multi-node configurations of the tBSN. **c** Operating principle and structural layout of the tBSN. The schematic shows signal transmission and magnetic coupling between the external reading coil and the textile-based sensor network. Photographs below illustrate the central hub antenna, interconnects, and local antenna of the tBSN. **d** Photograph of the AgNP-based flexible fiber electrode fabricated by the chemical via an in situ chemical formation process. **e** SEM image showing the uniform distribution of AgNPs on the surface of the fiber electrode. **f** Electrical resistance of the fiber electrode as a function of repeated in-situ formation cycles up to 5 cycles. **g** Durability test of the fiber electrode under 2000 bending cycles with a bending radius of 2.734 mm. Inset: magnified view of resistance changes during initial bending cycles.

differs from previously reported approaches in which flexible fiber electrodes are directly embroidered within the woven matrix of textiles, becoming a part of the textile architecture rather than being simply affixed onto the textile surface. Owing to the high flexibility and mechanical robustness of the fiber electrodes, various complex patterns, including textual characters, circular, rectangular, and heart-shaped spiral geometries, and arbitrary designs, were successfully realized on fabrics using this digital embroidery technique (Supplementary Fig. 6). In addition, with the excellent compatibility of the digital embroidery process, the fiber electrodes can be directly integrated onto a wide variety of off-the shelf textiles, including cotton, linen and nylon/polyurethane blend, using a typical embroidery process (Supplementary Fig. 7). The digital embroidery process enabled the precise and secure patterning of AgNP-based flexible electrodes onto conventional elastic textiles, forming a single-node sensor network comprising a hub antenna, a local antenna, and interconnects (Fig. 2b and Supplementary Fig. 8). Circular coils were adopted for both the hub and local antennas to enhance mechanical robustness and ensure stable inductive coupling. This geometry is advantageous as it reduces stress concentration during deformation and minimizes overall electrical resistance, which is a critical factor for enhancing a signal quality and durability of the textile-based body sensor network[42,43]. The single-node textile-based sensor network is capable of wirelessly capturing and transmitting responses from chip-less passive sensors aligned with the local antenna, as depicted in the equivalent lumped-circuit model presented in Fig. 2c. Specifically, when the passive wireless sensor exhibits capacitive or inductive changes in response to various types of external stimuli, the resultant shift is translated into a change in the resonant frequency (f_r) of the sensor network. This translation results from inductive coupling between the local antenna of the textile-based sensor network and the antenna within the passive sensor system (k_{ls} in Fig. 2c). The resonant frequency shift of the sensor network can be effectively detected through the inductive coupling between the network's hub antenna and an external reading coil connected to a network analyzer, which measures the S_{11} spectrum of the system (k_{rh} in Fig. 2c). The resonant frequency (f_r) of the textile-based sensor network, consisting of two antenna coils interconnected via conductive pathways, is predominantly determined by the total inductance (L) of the coils and their parasitic capacitance (C_p), as

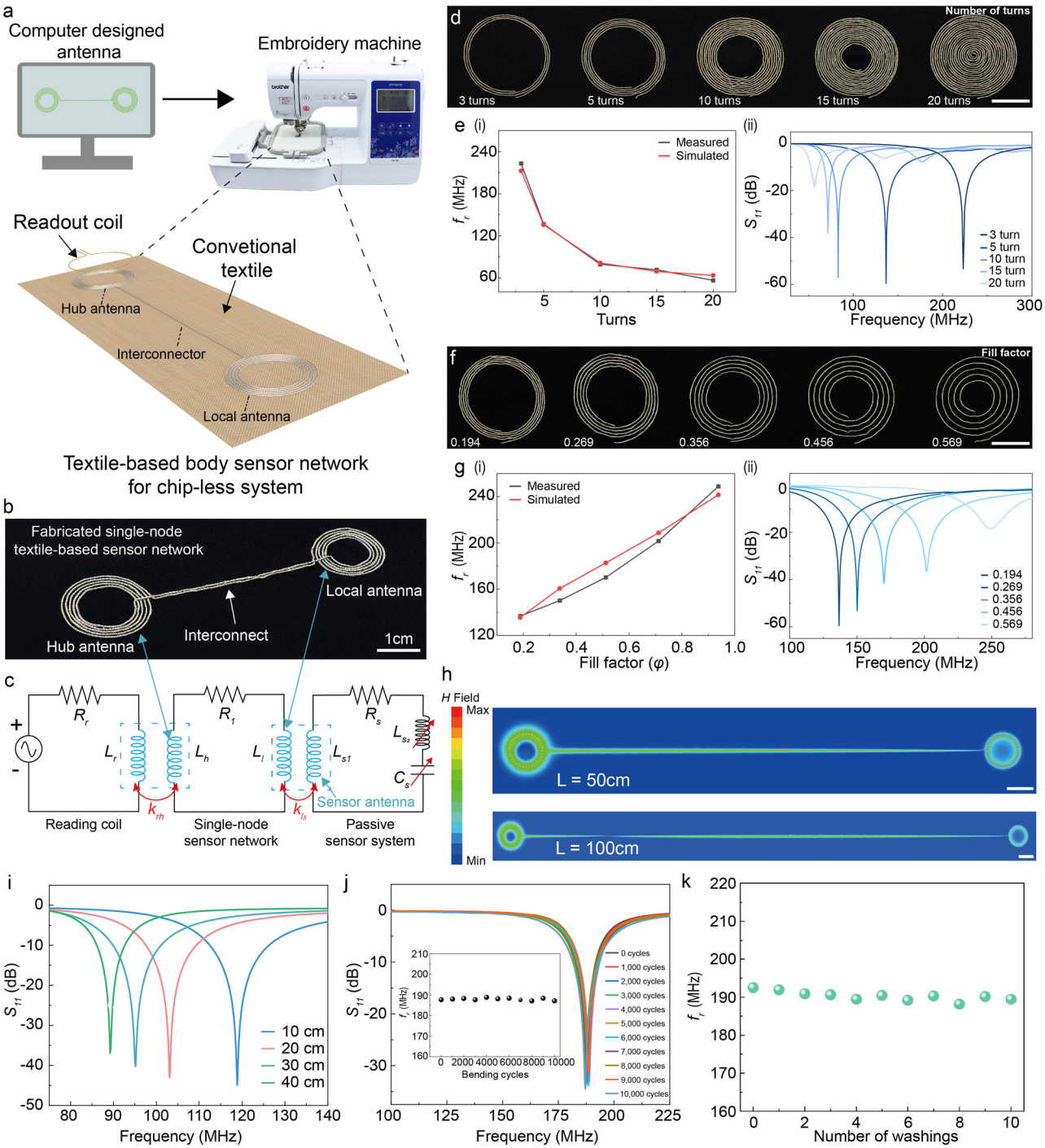

Fig. 2 | Electromagnetic and mechanical characterization of the single-node tBSN. a Schematic illustration of the digital embroidery process used to fabricate the textile-based body sensor network. Computer-designed antenna patterns are embroidered onto conventional textiles using a programmable embroidery machine. **b** Photograph of a single-node sensor network digitally embroidered on a textile substrate, consisting of a hub antenna, interconnect, and local antenna. **c** Lumped-element circuit model of the body sensor network coupled with an external reading coil and a passive sensor. The passive sensor may be capacitive and/or inductive, altering the resonant frequency of the network in response to external stimuli. **d** Photographs of textile-based antenna coils with varying numbers of turns (3, 5, 10, 15, and 20 turns), fabricated with a fixed outer diameter of 42 mm and turn spacing of 0.5 mm. Scale bar: 2 cm. **e** Electromagnetic performance of antenna coils with different numbers of turns: (i) Measured and simulated resonant frequencies as a function of the number of turns, and (ii) S_{11} spectra of the corresponding coils. **f** Photograph showing the textile-based antenna coil with varying fill factors (from left: 0.194, 0.269, 0.356, 0.456, 0.569), fabricated with a fixed outer diameter of 42 mm and 5 turns. Scale bar: 2 cm. **g** Electromagnetic performance of antenna coils with different fill factors: (i) Measured and simulated resonant frequencies as a function of fill factor, and (ii) Corresponding S_{11} spectra. **h** Simulated magnetic field distribution $|H|$ of the single-node sensor networks with interconnect lengths of 50 cm and 100 cm. Scale bar: 3 cm. **i** Measured S_{11} spectra of the single-node sensor networks with interconnect lengths of 10, 20, 30, and 40 cm. **j** S_{11} spectra of the textile-based sensor network under repeated bending deformation cycles up to 10,000 cycles at a bending radius of 4.5 mm. Inset: change in resonant frequency of the textile-based sensor network during repeated cyclic deformation up to 10,000 cycles. **k** Change in resonant frequency of textile-based sensor network during repeated washing cycles up to 10 rounds.

described by the following equation:

$$f_r = \frac{1}{2\pi\sqrt{LC_p}} \quad (1)$$

The geometric parameters of the antenna coils, including the number of turns, turn spacing, and inner and outer coil diameters, directly influence their inductance and parasitic capacitance, consequently affecting the resonant frequency of the sensor network[44]. To systematically investigate the effect of these geometric parameters on the electromagnetic properties of the textile-based antenna coils, a series of coils with varying numbers of turns (3–20 turns) but identical outer diameters (42 mm) and turn spacing (0.5 mm) were fabricated (Fig. 2d). Experimental results showed that increasing the number of turns from 3 to 20 reduced the resonant frequency from 223.15 to 56.49 MHz (Fig. 2e(i)), which is attributed to increases in both inductance and parasitic capacitance. These experimental results closely matched numerical simulation data. Effective detection of shifts in resonant frequency requires antenna coils with a high quality factor (Q-factor), which corresponds to sharper peaks in the S_{11} spectrum. The Q-factor of the sensor network is mathematically defined as:

$$Q = \frac{1}{R}\sqrt{\frac{L}{C_p}} \quad (2)$$

where R, L, and C_p indicate the resistance, inductance and parasitic capacitance of the antenna coil network, respectively. The geometric parameters of the antenna coils significantly impact their Q-factor. As shown in Fig. 2e(ii), the S_{11} spectra reveal that increasing the number of turns from 3 to 10 enhances the Q-factor, primarily due to the increased inductance (Supplementary Fig. 9). However, exceeding 10 turns resulted in a substantial degradation of the Q-factor of the antenna coil, due to the increased electrical resistance and parasitic capacitance resulting from the extended fiber electrode and the increased number of turns (Supplementary Fig. 10a), as predicted by Eq. (2). Nonetheless, even with decreased Q-factor, the antenna coils with more turns consistently exhibited clearly distinct resonant peaks, enabling reliable detection of resonant frequency shift. In addition to the number of turns, a fill factor (φ) of antenna coil, which quantifies the turn density in an antenna coil, was also investigated as shown in Fig. 2f. The fill factor is typically determined by the following equation[45]:

$$\varphi = \frac{(d_o - d_{in})}{(d_o + d_{in})} \quad (3)$$

where d_o and d_{in} denote the outer and inner diameter of the antenna coil, respectively. Higher fill factor of the antenna coil corresponds to larger turn spacing and lower density of turns in the coil. Figure 2g(i) shows the resonant frequency of the antenna coils having identical outer diameters (42 mm) and number of turns (5 turns), in response to increasing fill factor. As the fill factor of the antenna coil increased from 0.194 to 0.569, the resonant frequency of the coil also increased from 120.25 to 248.93 MHz due to reduced coil inductance. Conversely, the Q-factor of the antenna coil significantly decreased with increasing fill factor because the increased turn spacing significantly reduced the inductance of the coil (Fig. 2g(ii) and Supplementary Fig. 10b). Therefore, the antenna coil design can be effectively optimized by adjusting its geometric parameters to meet the requirements of specific target applications. Furthermore, to assess the effect of embroidery process on the mechanical properties of the textile, we performed uniaxial tensile tests on the textiles including embroidered antenna coil with varying densities (Supplementary Fig. 11). While higher embroidery density slightly increased stiffness of the textile system, the variation in mechanical properties could be ignored, and the overall stretchability or wearability of the textile showed no considerable degradation. This stability results from high mechanical compliance of the fiber electrodes embroidered onto the textile.

To reliably transmit sensor responses from distributed chip-less sensors across the body to the central hub antenna, the textile-based sensor network must maintain stable electromagnetic performance even when employing elongated interconnects. To investigate the effect of interconnect length on network performance, the magnetic field distribution and corresponding S_{11} spectra were numerically simulated for networks with interconnect lengths of 50 cm and 100 cm (Fig. 2h and Supplementary Fig. 12). The magnetic field at the hub antenna induced by the external reading coil effectively propagated to the local antenna, even through extended interconnects, verifying the capability of the sensor network for stable wireless signal transmission over elongated distances. Furthermore, the fabricated single-node textile-based sensor network demonstrated robust performance, exhibiting well-defined and stable peaks in the S_{11} spectra for diverse interconnect lengths ranging from 10 to 40 cm (Fig. 2i). Notably, both the resonant frequency and Q-factor of the sensor network remained stable following an intensive bending test of 10,000 cycles at a bending radius of 4.5 mm, demonstrating the high durability and mechanical robustness of the textile-based sensor network (Fig. 2j). This durability is primarily attributed to the mechanical and electrical stability of the flexible fiber electrodes, which include densely percolated AgNP networks firmly embedded within an elastomeric polymer matrix. Additionally, washing durability is one of the major concerns for ensuring the long-term usability of single-node textile-based sensor network in wearable applications. Based on the stable integration and encapsulation of fiber electrodes within the textile, the textile-based sensor network exhibited no significant changes in resonant frequency after 10 washing cycles conducted according to the ISO 6330 standard, which involved mechanical agitation in a domestic washing machine with 2 kg of clothing and standard detergent, followed by washing, rinsing and spinning steps, confirming its suitability for daily wear (Fig. 2k and Supplementary Fig. 13). Furthermore, the single-node textile-based sensor network maintained stable electromagnetic performance under varied environmental temperatures ranging from 25 °C to 40 °C and various external mechanical pressures applied directly onto its local antenna (Supplementary Figs. 14 and 15). To enable use of the textile-based antenna system in wearable applications, skin compatibility of tBSN is essentially required. Accordingly, we performed a skin irritation test to evaluate skin-contact safety of the textile-based antenna coil by directly attaching it to the forearm using a medical adhesive film for 12 h. As shown in Supplementary Fig. 16, no signs of skin irritation, redness or discomfort were observed after the long direct contact between the textile-based antenna coil and skin, demonstrating its excellent skin compatibility. This is attributed to the full encapsulation of the AgNP-based fiber electrode with a biocompatible SEBS coating layer, which serves as a robust barrier preventing direct contact between the AgNPs and the skin. To further investigate the effects of perspiration on the tBSN, phosphate-buffered saline (PBS) was applied to the local antenna of the single-node tBSN to simulate sweat exposure (Supplementary Fig. 17). Compared to the dry condition, the presence of PBS induced changes in the S_{11} spectra, including peak broadening and attenuation. These effects likely arise from PBS, which has a high dielectric constant, being absorbed into spaces between the traces of the coil. The presence of PBS increased the parasitic capacitance of the antenna, resulting in a decrease in both the quality factor and resonant frequency of the single-node tBSN. Nevertheless, the resonant peaks remained clearly distinguishable, allowing for reliable tracking of frequency shifts. Collectively, these excellent stabilities ensure the robustness, durability, and practical feasibility of the textile-based sensor network for advanced wearable applications.

Concentric multi-nodes textile-based body sensor network

For practical wearable body sensor networks (BSNs), single-node textile-based sensor networks must be extended to multi-node configurations capable of simultaneously monitoring passive wireless responses from sensors distributed across the body. To achieve this, we designed multiple hub antennas, each serving as a single-node sensor network, of varying sizes and arranged them in a concentric layout. In this concentric configuration,

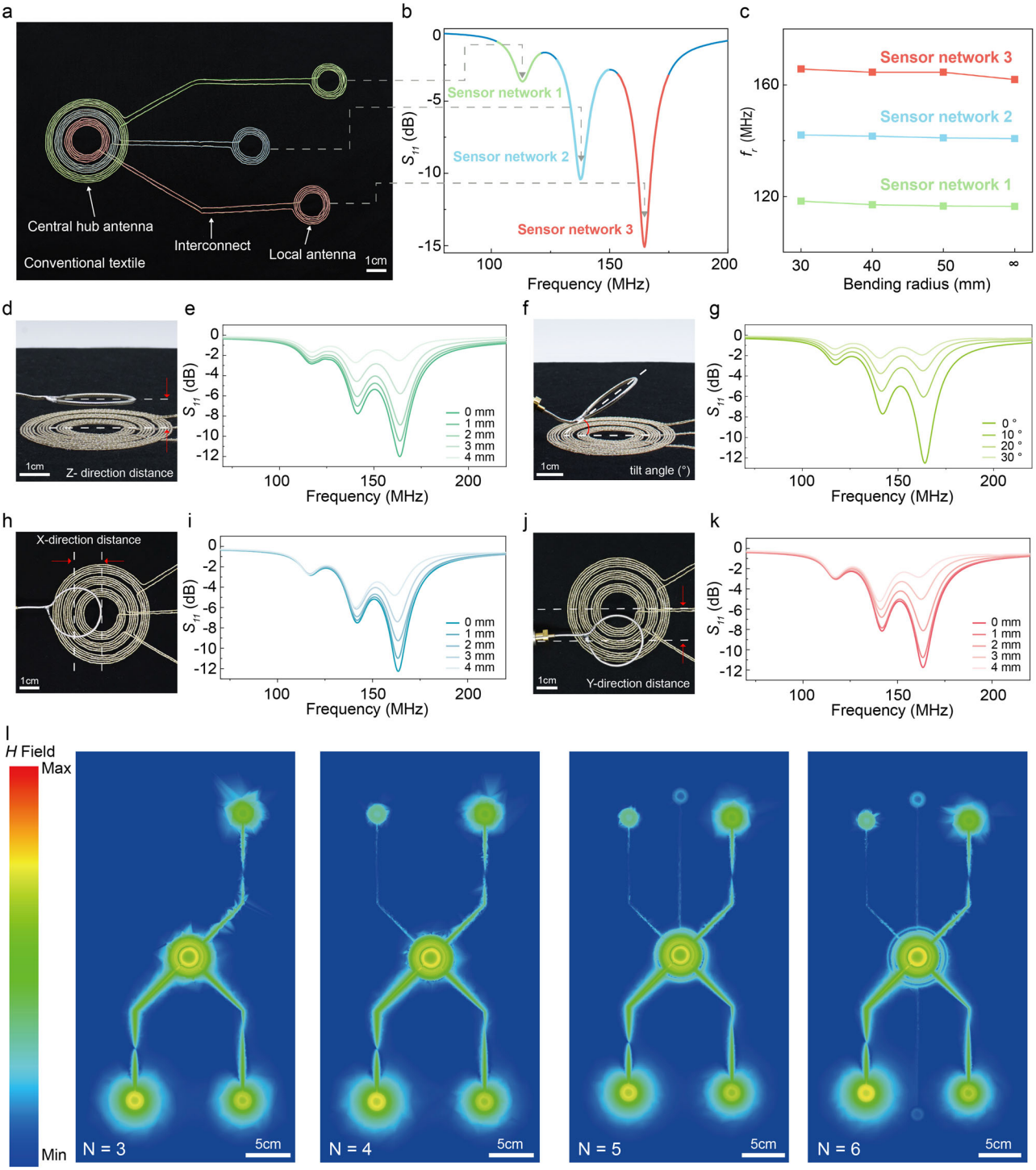

Fig. 3 | Multi-node tBSN enabled by a concentric multi-hub antenna design. **a** Photograph of the fabricated tBSN consisting of three concentric single-node sensor networks, each with a distinct hub antenna diameter. **b** S_{11} spectra showing well-separated resonant peaks for each sensor network node in the tBSN. **c** Resonant frequency of each sensor network under bending deformation with varying bending radii. **d** Photograph showing vertical (z-direction) separation between the external reading coil and the hub antenna. **e** S_{11} spectra of the tBSN as a function of increasing vertical separation distance between the reading coil and the tBSN. **f** Photograph showing angular misalignment between the reading coil and the hub antenna. **g** S_{11} spectra of the tBSN as a function of increasing angular misalignment (0°–30°). **h** Photograph showing lateral misalignment along the x-direction between the reading coil and hub antenna. **i** S_{11} spectra of the tBSN as a function of increasing x-direction misalignment (0–4 mm). **j** S_{11} spectra of the tBSN as a function of increasing x-direction misalignment (0–4 mm). **k** S_{11} spectra of the tBSN corresponding to increasing y-directional displacement (0–4 mm). **l** Simulated $|H|$ of the tBSN with increasing numbers of concentric single-node sensor networks ($N = 3$ to 6), showing spatially distinct magnetic hotspots at each local antenna. Scale bar: 5 cm.

the hub antennas collectively function as the central hub antenna for the textile-based BSN (tBSN), enabling wireless, simultaneous, and selective detection of resonant-frequency shifts from each node within a single frequency scan (Supplementary Fig. 18). Figure 3a presents a photograph of the tBSN, in which three single-node sensor networks, each with a different hub antenna diameter, are concentrically arranged on a textile substrate. The concentric configuration results in three discrete resonant frequencies, at 113.29, 137.80, and 164.79 MHz, clearly separated in the S_{11} spectrum (Fig.

3b). This frequency multiplexing ensures that each sensor node can be uniquely identified and wirelessly interrogated within a single scan. To determine the optimal reading coil geometry for the simultaneous readout of all nodes in the concentric multi-node tBSN, we fabricated three reading coils with different diameters (2.4 cm, 3.8 cm, and 5.2 cm) and evaluated their wireless coupling performance by measuring S_{11} spectrum of the multi-node tBSN as shown in Supplementary Fig. 19. The results showed that the 2.4 cm diameter reading coil, which matches the diameter of the innermost hub antenna (sensor network 3), exhibited the well-defined resonant peaks across all sensor networks. To ensure clear and distinct resonance peaks for all three sensor networks, a circular external reading coil with a diameter matching that of the smallest hub antenna was employed. For practical applications of the tBSN in daily life, mechanical robustness and stability of the network must be ensured. To this end, the S_{11} spectra of the tBSN were evaluated under bending deformation with varying bending radii (Supplementary Fig. 20). Despite the diverse bending deformations, the resonant frequencies of all three sensor networks in the tBSN remained stable, demonstrating the system's tolerance to mechanical stress (Fig. 3c). To investigate the effects of on-body dielectric loading on the tBSN, the S_{11} spectrum of both single-node and multi-node tBSN were measured while attached to human skin as shown in Supplementary Fig. 21. While electromagnetic performance of the tBSN was slightly detuned by the dielectric properties of the human body, both single-node tBSN and multi-node tBSN maintained clearly distinguishable resonant peaks enabling reliable identification of individual sensor nodes.

In realistic scenarios, dynamic body movements may cause misalignment between the external reading coil and the tBSN's central hub antenna, affecting coupling efficiency and signal clarity. The coupling efficiency can be quantified by a coupling coefficient (k) between the reading coil and hub antenna, defined by Eq. (4)[46].

$$k = \frac{M}{\sqrt{L_1 L_2}} \tag{4}$$

where M represents the mutual inductance between the hub antenna and reading coil, and L_1 and L_2 are the self-inductances of each component, respectively. Misalignments reduce the mutual inductance, thereby lowering the coupling efficiency and diminishing the prominence of the resonance peaks in the S_{11} spectrum. To experimentally investigate the effect of the misalignments, we measured the S_{11} spectrum of the tBSN under controlled misalignments in the z-direction (vertical separation), tilt angle, lateral x- and y-directions (Fig. 3d, f, h, j). The misalignment limits were conservatively chosen considering the minimal garment displacement typically observed in tight-fitting apparel during daily use. The sharpness of the resonance peaks decreased with increasing vertical separation and tilt angle between the two coils (Fig. 3e, g), a result attributed to reduced mutual inductance and coupling efficiency. Interestingly, x- and y-directional misalignments caused asymmetrical degradation of the resonance peaks of the tBSN, as shown in Fig. 3i, k. This behavior can be attributed to different overlapping areas between the reading coil and each concentric hub antenna. The innermost hub antenna coil corresponding to sensor network 3 exhibited the highest sensitivity to misalignment, as lateral displacement of the reading coil substantially reduced its overlapping area with the smaller antenna. In contrast, the outermost hub antenna for sensor network 1 maintained strong inductive coupling, since the larger coil continued to encompass the reading coil even under misaligned conditions. This spatial dependence provides a potential design advantage for prioritized sensing where alignment is variable during motion. Despite reduced signal intensity under misaligned conditions, all three sensor networks in the tBSN stably retained their bell-shaped resonant peak responses and resonant frequencies, demonstrating robust wireless performance across intensive misalignment conditions, including separation distances up to 4 mm, tilt angles up to 30°, and misalignments in the x- and y-directions up to 4 mm (Supplementary Fig. 22). These results confirm that the tBSN can operate reliably under various misalignments commonly encountered during daily activities. Additionally, while inductive coupling strength diminishes with coil-to-coil distance and misalignment, this spatial dependence also serves as a benefit by minimizing unintended signal interference between nearby users, as effective signal coupling requires close alignment in both position and orientation.

To further investigate the system's scalability, we simulated magnetic field distributions as the number of concentric single-node sensor networks increased from 3 to 6 (Fig. 3l). A single readout coil positioned at the center of the tBSN generated distinct magnetic hotspots at the location of each local antenna, confirming the ability to deliver and retrieve signals across multiple nodes. Although field strength decreased with increasing node count due to extended transmission paths and weaker coupling at the periphery, all sensor networks retained distinct and stable resonant responses, as confirmed by S_{11} spectra in Supplementary Fig. 23. These results demonstrate the scalability and reliability of tBSN for simultaneous multi-node sensing within a compact, textile-integrated platform.

Multi-node demonstration of tBSN garments for wireless, chip-less biomechanical sensing

Given the high performance and stability of the system, the tBSN was demonstrated as a chip-less and wireless textile-based body sensor network garment for physical motion monitoring. Figure 4a presents a schematic illustration depicting the stretching of the vastus lateralis (VL) and knee bending during gait motion. The VL is one of the four quadriceps muscles in the thigh and is primarily responsible for knee extension. It works in conjunction with the other quadriceps femoris muscles to extend the knee during activities such as walking, running, and jumping, and is therefore critically important in gait motion and rehabilitation[47–49]. Furthermore, the VL plays a key role in stabilizing the knee joint, working with the vastus medialis to ensure proper patellar tracking and to prevent excessive lateral displacement. Dysfunction in the VL can lead to impaired balance, increased knee pain, and abnormal gait patterns, which may cause further musculoskeletal complications[50,51]. Therefore, real-time monitoring of VL movement in relation to knee bending can offer comprehensive insight into functional movement patterns and rehabilitation progress during gait and exercise.

To demonstrate effective monitoring of VL movement and knee motion, we fabricated a flexible, chip-less, and wireless passive strain sensing system based on a fiber-type capacitive strain sensor (Supplementary Fig. 24). The capacitive response of the fiber-based strain sensor could be wirelessly recorded by tracking the shifts in the resonant frequency of the sensing system using a network analyzer (Supplementary Fig. 25). To evaluate the sensitivity of the single-node tBSN coupled with the passive strain sensor, we systematically applied tensile strain from 0% to 40% to the strain sensor while monitoring the corresponding changes in the S_{11} spectra of the single-node tBSN (Supplementary Fig. 26). The resonant frequency shifted gradually with increasing strain, exhibiting two distinct sensitivities of −347 kHz/% strain and −155 kHz/% strain in the low- and high-strain regions, respectively. This two-stage behavior is explained by the intrinsic working mechanism of the fabricated strain sensor, as previously reported[52]. In addition, tensile strain of 0.5% was still detectable through distinguishable frequency shifts in the single-node tBSN (Supplementary Fig. 27). Furthermore, while signal attenuation occurred with increasing vertical distance between the hub antenna and reading coil, the single-node tBSN maintained a bell-shaped resonance peak and resonant frequency (Supplementary Fig. 28a). Within this range, the single-node tBSN consistently captured strain-induced frequency shifts from the coupled passive sensor, confirming its reliable wireless readability (Supplementary Fig. 28b–d). To evaluate the potential for simultaneous monitoring of multiple passive sensors within a single frequency scan, we fabricated a tBSN consisting of two single-node sensor networks and coupled each with an individual chip-less, passive strain sensor positioned on each local antenna (Supplementary Fig. 29). Figure 4b shows the measured S_{11} spectrum of the dual-node tBSN coupled with the two strain sensors, exhibiting distinct resonant

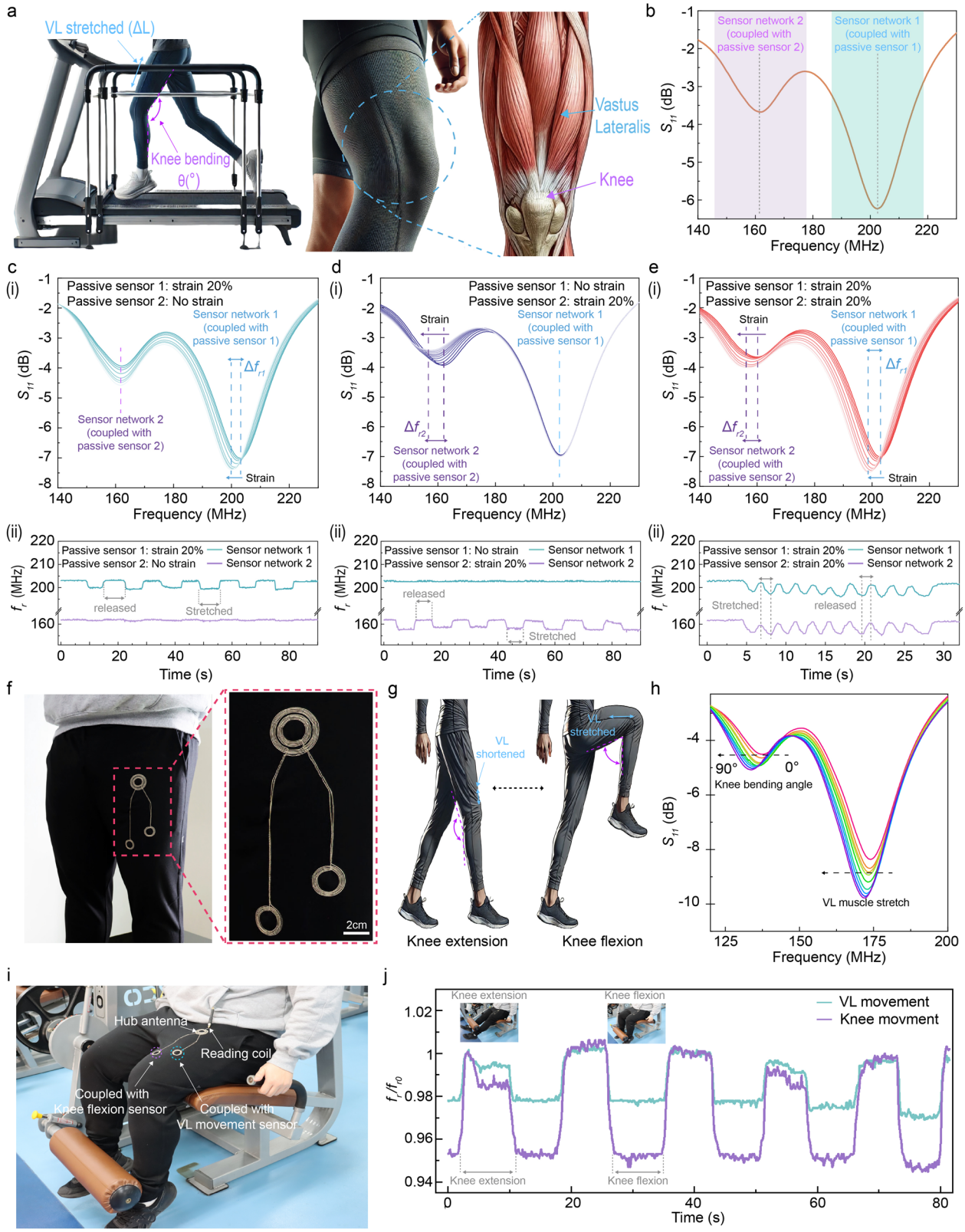

frequencies at 160.00 MHz and 202.65 MHz. These resonant frequencies were selectively shifted depending on the capacitive response of each passive strain sensor attached to the local antennas (Supplementary Note). Based on this operating principle, we successfully monitored the wireless responses of both strain sensors by tracking the shifts in their respective resonant frequencies (Fig. 4c(i), d(i), (i)). It is noteworthy that the entire sensor network system, including the distributed body sensors, contains no conventional semiconductor chips, as both the network and sensors rely entirely on passive components such as resistors, capacitors, and inductors. Furthermore, Fig. 4c(ii), d(ii) demonstrate stable tracking of the resonant frequency shifts induced by the two passive strain sensors, with minimal crosstalk. This confirms that the fabricated tBSN enables

Fig. 4 | Wireless monitoring of biomechanical movements via tBSN-integrated garments. a Schematic illustration depicting the role of the vastus lateralis (VL) muscle in knee motion and gait rehabilitation. **b** Measured S_{11} spectra of the tBSN system coupled with two chip-less passive strain sensors, showing distinct resonant peaks corresponding to each sensor. **c–e** Wireless monitoring of sensor responses through the tBSN when one or both sensors are strained. (i) S_{11} spectra showing frequency shifts for three conditions (left to right): strain applied to the passive sensor on sensor network 1, sensor network 2, and both networks simultaneously. (ii) Continuous tracking of resonant frequency shifts under the same three conditions, confirming independent and simultaneous monitoring of the passive sensors with minimal crosstalk. **f** Photograph of the tBSN garment with two local antenna coils positioned near VL and knee regions without the affixed passive strain sensor. **g** Schematic illustration showing the biomechanical relationship between VL muscle dynamics and knee joint motion. **h** S_{11} spectra of the tBSN garment under strain applied to both VL and knee regions during knee flexion, indicating clear and distinguishable frequency responses. **i** Photograph showing an experimental setup for real-time monitoring of VL and knee movement during leg extension exercise using the tBSN garment. **j** Normalized resonant frequency changes corresponding to repeated cycles of knee extension and flexion, showing synchronized response of the two sensor nodes.

multi-node, wireless monitoring of passive sensors distributed across the body without interference between the sensor nodes. In addition, Fig. 4e(ii) shows that the tBSN maintains accurate tracking of frequency shifts even when both sensors are strained simultaneously, with no significant interference observed.

To demonstrate the potential of the tBSN as a wearable, chip-less body sensor network, we integrated the two-node sensor network system into a garment capable of continuously monitoring biomechanical signals from distributed passive sensors. Specifically, the tBSN was embroidered onto polyester-rayon pants, with two antenna coils placed near the VL and knee regions (Fig. 4f). Simultaneous sensing of the VL and knee is important for gait and lower-limb analysis, as knee flexion and extension directly correlate with VL elongation and isometric contraction, respectively (Fig. 4g). To verify the correlation between VL movement and knee motion, we coupled the tBSN garments with two passive strain sensors affixed to the VL and knee location (Supplementary Fig. 30). As shown in Fig. 4h, both knee bending and the corresponding VL muscle stretching were successfully monitored by measuring the shifts in resonant frequencies of the two sensor networks in the tBSN coupled with the two passive sensors. The decreased resonant frequencies of the two sensor networks resulted from increased capacitances in the two passive strain sensors stretched under biomechanical deformation. Furthermore, the tBSN garments were demonstrated as a fitness and rehabilitation-assistive platform by monitoring VL and knee behavior during a leg extension exercise (Fig. 4i). The tBSN garment successfully monitored the repetitive cycles of knee flexion and VL extension during exercise (Fig. 4j). To further explore the real-world applicability of the system, we evaluated the tBSN garment during treadmill walking, a representative scenario of daily locomotion (Supplementary Fig. 31). The tBSN garment, coupled with two passive sensors, successfully tracked both knee movement and VL muscle dynamics during natural gait, with clearly distinguishable and reproducible shifts in resonant frequencies corresponding to each sensor. To further investigate the sensing performance of the tBSN under dynamic conditions, a single-node tBSN garment coupled with a passive strain sensor affixed at the knee location was evaluated during various dynamic activities including repeated knee flexion, slow walking, normal walking, and running (Supplementary Fig. 32). Despite increased signal fluctuations of the tBSN during the dynamic activities, the tBSN garment could consistently track the knee movement with distinct resonant frequency shifts across all tested motions, demonstrating high performance in wearable applications.

Discussion

In summary, we developed an all-textile, chip-less, and battery-free body sensor network capable of wireless and simultaneous monitoring of multiple passive sensors distributed across various body locations. To fabricate the tBSN, flexible conductive fiber electrodes were fabricated by embedding AgNPs into the SBS polymeric matrix coated onto the fiber scaffold. The fabricated flexible conductive fiber electrodes exhibited a low electrical resistance of 0.22 Ω/cm and maintained high stability over 2000 bending cycles. Textile-based single-node body sensor networks were seamlessly fabricated on conventional elastic fabrics by digitally controlled embroidery of the fiber electrodes, exhibiting robust wireless electromagnetic transmission even with elongated interconnect lengths of up to 40 cm. By arranging multiple single-node sensor networks into a concentric hub antenna architecture, we successfully extended the design to a multi-node tBSN. The fabricated multi-node tBSN exhibited stable electromagnetic performance irrespective of the number of sensor networks, even under various misalignment conditions between the external reading coil and the central hub antenna. In addition, the tBSN successfully maintained its inductive coupling and electromagnetic stability under repeated bending deformation, varying environmental temperatures, and external mechanical pressures, demonstrating high durability and stability. We demonstrated that the tBSN could be seamlessly integrated into wearable garments for simultaneous monitoring of biomechanical signals from the VL muscle and knee joint during diverse movements, using passive strain sensors. Although our results provide the significant potential of this chip-less and textile-based sensor network platform for personalized rehabilitation, fitness-assistive technologies, and advanced gait analysis, the current reliance on a bulky VNA limits its wearable practicality. To address this issue, the bulky readout module could be replaced by a portable, miniaturized, and lightweight system, enabling the realization of fully wearable and user-friendly sensing platforms. These efforts will also support future validation with practitioners for biomedical applications, ultimately facilitating the transition of the tBSN system in real-world applications. Additionally, to support system scalability across a larger body area, our future work also will focus on mitigating mutual interference through the implementation of electromagnetic shielding, enhancing long-term signal quality via passivation and encapsulation of fiber electrodes and textiles, and improving mechanical comfort through structural optimization.

Methods

Fabrication of AgNP-based flexible fiber electrode

An Ag-based flexible fiber electrode was fabricated using an in-situ formation process, wherein Ag ions were absorbed into a polymeric matrix and subsequently reduced to form Ag nanoparticles. Commercialized nylon threads, with a denier of 100 were dip-coated with 20 wt% SBS (432490, beads, Sigma-Aldrich) was dissolved in tetrahydrofuran (CAS. No. 109-99-9, DAEJUNG) to create a polymeric matrix. After coating, the SBS-coated nylon threads were annealed overnight in a 60 °C oven. The annealed SBS-coated Nylon threads were immersed in 20 wt% solution of AgCF3COO (Sigma-Aldrich Corp., CAS 2966-50-9) in ethanol for 30 min to absorb a large amount of Ag+ ions into the polymeric layer, followed by air drying for 20 min. Subsequently, to reduce Ag+ ions into Ag nanoparticles, the SBS/precursor composite-coated Nylon fiber was immersed in an ascorbic acid (Sigma-Aldrich Corp., CAS 50-81-7) solution in DI water (5 wt%) for an hour in a 60 °C oven. After an hour, SBS/AgNPs coated Nylon fiber was washed with Di water to eliminate residual reducing agents and dried in the air for an hour. Fabricated AgNP-based flexible fiber electrode was dip-coated with a 20 wt% SEBS powder (66070-58-4, powder, average Mw ≈ 118,000, Sigma-Aldrich) dissolved in cyclohexane (179191, ≥99.0%, Sigma-Aldrich) for the encapsulation layer. After a dip-coating process, the AgNP-based flexible fiber electrodes were annealed overnight in a 60 °C oven.

Characterization and optimization of the flexible fiber electrode

Electrical stability under bending deformation was assessed by employing a custom-designed bending stage to apply mechanical stress to the AgNP-

based fiber electrode while concurrently measuring its electrical resistance with an inductor-capacitor-resistor (LCR) meter (E4980AL, Keysight Technologies Inc.). A field emission scanning electron microscope (S-4800, Hitachi Inc.) equipped with an EDS module (Hitachi Inc.) was utilized to investigate the surface morphologies of the AgNP-based fiber electrode, capturing both SEM and EDS mapping images.

Fabrication of textile-based body sensor network

The tBSN was designed using commercial software (PE-DESIGN 10, Brother) as a stitch trajectory and uploaded to a digital embroidery machine (NV180, Brother). The lubricant was applied to the AgNP-based flexible fiber electrode to ensure smooth embroidery by eliminating the sticky properties on its surface. Before the embroidery, the fabricated AgNP-based flexible fiber electrode was uniformly wound onto a bobbin using a bobbin winder. After winding a flexible fiber electrode onto a bobbin, the bobbin was loaded onto the embroidery machine as a sewing thread, while a commercialized nylon fiber was loaded onto the embroidery machine as a supporting thread. A wash-away sewing stabilizer was applied during the embroidery process to prevent wrinkles and ensure a flat textile-based antenna coil. For the embroidery process, the flexible fiber electrode was digitally embroidered onto cotton-spandex fabric or cotton-polyurethane shirts, following a computer-controlled design pattern. The embroidery machine moves according to a pre-designed stitch path, synchronizing the movement of the needle with the X-Y position of the fabric to form an interlocking stitch between the upper support thread and the bobbin conductive thread. Additionally, using a digital embroidery machine allows for the precise transfer of fiber electrodes onto fabric, enabling the implementation of complex designs that require high flexibility due to the exceptional flexibility of the fiber electrodes (Fig. S5). The thermal silver paste (ELCOAT P-100, CANS) was used for the connection of flexible fiber electrodes and subsequently cured for 2 h in a 60 °C oven. The Ecoflex 0010 (Smooth-on Inc.) was used to seal the connection area. The Ecoflex solution was prepared by mixing the base and corresponding curing agent in a 1:1 weight ratio using a speed mixer (ARE-310, THINKY) at 2000 rpm for 2 min, followed by degassing in a desiccator cabinet for 3 min to remove air bubbles. After preparation, the mixture was coated to the connection area and cured for 4 h in a 60 °C oven.

Characterization of the textile-based body sensor network

The S_{11} of the sensor network was measured using an ENA network analyzer (Keysight E5063A) with a custom-made readout coil. When measuring the resonance frequency of the antenna coil, the vertical distance between the antenna coil and the readout coil was fixed at 1 mm. The bending test was conducted by clamping both ends of the body sensor network on a custom-designed bending stage. The tBSN was repeatedly bent using a custom-made bending stage for 10,000 cycles, and its S_{11} parameter was recorded every 1000 cycles. The washability test was conducted according to the ISO 6330 standard, which involved mechanical agitation in a domestic washing machine with 2 kg of clothing and standard detergent, followed by washing, rinsing, and spinning steps. After each washing cycle, the S_{11} parameter of the tBSN was measured. The thermal stability test of the system was verified by allowing it to stabilize for 1 h at each specified temperature, ensuring thermal equilibrium before measurements were conducted. To verify durability under pressure, the system was placed on a motorized z-axis stage equipped with a force gauge, and a cyclic pressure of 10,000 N/m^2 was applied to the system's sensor nodes. The S_{11} of the system was recorded after the mechanical deformations. The misalignment effect between the readout coil and the system's hub antenna was measured by placing the system on a custom x-stage machine while the readout coil was fixed in a clamp.

Numerical simulation

A finite element analysis was conducted to numerically assess the magnetic field and scattering parameters (S-parameters) of the antenna. The magnetic field, denoted as H, is derived from Maxwell's equations using the relationships in Eqs. (1) and (2):

$$H = \frac{j}{\omega\mu}\nabla \times E \tag{1}$$

$$\nabla \times (\nabla \times E) - \mu\varepsilon\omega^2 E = 0 \tag{2}$$

Here, E represents the electric field, ω is the angular frequency μ is the permeability, and ε is the permittivity. The simulation model of the wireless reader, constructed in copper with a diameter of 0.3 mm, was assigned a lumped port impedance of 50 Ω. For the conductive fibers, the coil was modeled with a diameter of 0.5 mm and an electrical conductivity of 169,765 S/m. The permeability and the permittivity were set to 1 and 4, respectively, with a measured frequency of 9.4 GHz. These parameters were determined from experimental data. The commercial software ANSYS High-Frequency Structure Simulator (HFSS) was employed to numerically solve Eqs. (1) and (2). HFSS discretizes the structure into tetrahedral elements to compute the electromagnetic field, yielding the magnetic field distribution and S-parameters. Radiation boundary conditions were applied to reduce artificial reflections, and due to the model's complexity, an adaptive meshing was utilized to dynamically adjust element sizes, ensuring convergence criteria were met.

Fabrication of the AgNP-based stretchable fiber electrode for fiber strain sensor

An Ag-based stretchable fiber electrode was fabricated using an in-situ formation process. The polyurethane-based stretchable fiber matrix purchased from Taekwang was immersed in a 35 wt% solution of AgCF3COO (Sigma-Aldrich Corp., CAS 2966-50-9) in ethanol for 30 min to absorb a large amount of Ag+ ions into the polymeric layer, followed by air drying for 20 min. Subsequently, to reduce Ag+ ions into Ag nanoparticles, the fiber was immersed in an ascorbic acid (Sigma-Aldrich Corp., CAS 50-81-7) solution in DI water (2 wt%). Following this reduction process, the fiber was thoroughly rinsed with deionized water to eliminate any residual materials and then air-dried for an additional hour.

Fabrication of the fiber-based capacitive strain sensors

The fiber-based capacitive strain sensors were fabricated by placing two conductive fiber electrodes to double helical structure with a hollow core, as previously reported[53]. The surface of the fabricated Ag-based stretchable fiber electrode was encapsulated with a thin layer of Ecoflex 0010 (Smooth-On Inc.) to prevent electrical shorting when the capacitive strain sensor is fully stretched. The Ecoflex solution was prepared by mixing the base and curing agent in a 1:1 weight ratio. The Ecoflex solution was carefully applied to the vertically stabilized fiber. After allowing it to set for an additional 10 min, the fiber electrode coated with the Ecoflex solution was placed in an oven at 80 °C for 10 min to cure the elastomeric layer. The coated fiber electrode was then wound into a double helical structure around a sacrificial core wire, followed by successive coating of Ecoflex 00-10 to secure the double helical configuration. The coated helical structure was again annealed in the oven at 80 °C for 10 min. Finally, the sacrificial core wire was extracted by pulling it out while holding onto the helical structure. The capacitance of the fiber strain sensor effectively increases with a rapid decreasing the distance between the two double helical fiber electrodes under external strains applied to the sensor, as previously reported[53].

Fabrication of the chip-less wireless strain sensor

The textile-based antenna coil was designed using commercial software (PE-DESIGN 10, Brother) as a stitch trajectory and uploaded to a digital embroidery machine (NV180, Brother). The AgNP-based flexible fiber electrode was digitally embroidered onto a cotton-spandex fabric, following a pre-designed antenna coil pattern. Once the embroidery process was completed, the textile-based antenna coil and the capacitive strain sensor were connected using a thermal silver paste (ELCOAT P-100, CANS) and

subsequently cured in a 60 °C oven for 2 h. The Ecoflex 0010 (Smooth-on Inc.) was used to seal the connection area to prevent electrical shorting.

Simultaneous monitoring of the knee flexion and VL movement

Knee flexion and VL movement were assessed in a human subject wearing the tBSN garment. The tBSN garment incorporates two textile-based sensor networks. Sensor network 1 consists of an interconnector with a length of 8.6 cm, a hub antenna (outer diameter: 2.6 cm, fill factor: 0.2, 5 turns), and a local antenna (fill factor: 0.2, 5 turns). Sensor network 2 consists of an interconnector with a length of 10.4 cm, a hub antenna (outer diameter: 3.8 cm, fill factor: 0.14, 5 turns), and a local antenna (fill factor: 0.2, 5 turns). One healthy adult volunteer participated in this study. The participant received a detailed explanation of the experimental procedure and voluntarily provided written informed consent prior to participant. To measure knee flexion and VL movement, two chip-less wireless strain sensors were sewn into a thigh band and positioned directly on the VL and knee, respectively. The two local antennas of the textile-based BSN garment were aligned with the antenna coils of the chip-less wireless strain sensors, ensuring seamless data transmission. In the experimental setup, the reading coil was placed in vertical alignment with the central hub antenna at a distance of about 1 mm. During knee flexion, continuous reflection coefficient measurement was performed using a Python-based data logging system, which recorded reflection coefficient values at 0.1-s intervals.

Data availability

Data is provided within the manuscript or supplementary information files.

Code availability

All codes that support the findings of this study are available from the corresponding authors upon reasonable request.

Received: 26 May 2025; Accepted: 12 September 2025;
Published online: 04 November 2025

References

1. Gao, Y. et al. Flexible hybrid sensors for health monitoring: materials and mechanisms to render wearability. *Adv. Mater.* **32**, 1902133 (2020).
2. Tian, G. et al. Hierarchical piezoelectric composites for noninvasive continuous cardiovascular monitoring. *Adv. Mater.* **36**, 2313612 (2024).
3. Zhu, X. et al. A robust near-field body area network based on coaxially-shielded textile metamaterial. *Nat. Commun.* **15**, 6589 (2024).
4. Wang, K. et al. Smart wearable sensor fuels noninvasive body fluid analysis. *ACS Appl. Mater. Interfaces* **17**, 13279–13301 (2025).
5. Trung, T. Q. et al. Flexible and stretchable physical sensor integrated platforms for wearable human-activity monitoringand personal healthcare. *Adv. Mater.* **28**, 4338–4372 (2016).
6. Janićijević, Ž et al. Design and development of transient sensing devices for healthcare applications. *Adv. Sci.* **11**, 2307232 (2024).
7. Zhang, X. et al. Stretchable and robust all-in-one tribovoltaic textile for sport and fitness tracking. *Adv. Fiber Mater* **7**, 926–936 (2025).
8. Li, Y. et al. Metal-organic framework-based tribovoltaic textile for human body signal monitoring. *Adv. Sci*. **12**, 2414086 (2025).
9. Lee, S. et al. Nanomesh pressure sensor for monitoring finger manipulation without sensory interference. *Science* **370**, 966–970 (2020).
10. Leber, A. et al. Thermally drawn elastomer nanocomposites for soft mechanical sensors. *Adv. Sci.* **10**, 2207573 (2023).
11. Han, J. et al. Synergistic strategies of biomolecular transport technologies in transdermal healthcare systems. *Adv. Healthc. Mater.* **13**, 2401753 (2024).
12. Wang, W. et al. Janus membrane-based wearable pH sensor with sweat absorption, gas permeability, and self-adhesiveness. *ACS Appl. Mater. Interfaces* **16**, 27065–27074 (2024).
13. Khan, Y. et al. Monitoring of vital signs with flexible and wearable medical devices. *Adv. Mater.* **28**, 4373–4395 (2016).
14. Seshadri, D. R. et al. Wearable sensors for monitoring the physiological and biochemical profile of the athlete. *npj Digit. Med.* **2**, 72 (2019).
15. Qin, H. et al. Laser-induced graphene-based smart textiles for wireless cross-body metrics. *ACS Appl. Nano Mater.* **6**, 19158–19167 (2023).
16. Yuce, M. R. Implementation of wireless body area networks for healthcare systems. *Sens. Actuators A: Phys.* **162**, 116–129 (2010).
17. Chu, B. et al. Bring on the bodyNET. *Nature* **549**, 328–330 (2017).
18. Lin, R. et al. A DIY approach to wearable sensor networks. *Nat. Electron.* **4**, 771–772 (2021).
19. Hasan, K. et al. A comprehensive review of wireless body area network. *J. Netw. Comput. Appl.* **143**, 178–198 (2019).
20. Lee, K. et al. Mechano-acoustic sensing of physiological processes and body motions via a soft wireless device placed at the suprasternal notch. *Nat. Biomed. Eng.* **4**, 148–158 (2020).
21. Kim, Y.-S. et al. Soft wireless bioelectronics designed for real-time, continuous health monitoring of farmworkers. *Adv. Healthc. Mater.* **11**, 2200170 (2022).
22. Chung, H. U. et al. Binodal, wireless epidermal electronic systems with in-sensor analytics for neonatal intensive care. *Science* **363**, eaau0780 (2019).
23. Hajiaghajani, A. et al. Textile-integrated metamaterials for near-field multibody area networks. *Nat. Electron.* **4**, 808–817 (2021).
24. Niu, S. et al. A wireless body area sensor network based on stretchable passive tags. *Nat. Electron.* **2**, 361–368 (2019).
25. Amendola, S. et al. RFID technology for IoT-based personal healthcare in smart spaces. *IEEE Internet Things J.* **1**, 144–152 (2014).
26. Fang, Y. et al. A deep-learning-assisted on-mask sensor network for adaptive respiratory monitoring. *Adv. Mater.* **34**, 2200252 (2022).
27. Liu, Y. et al. Electronic skin as wireless human-machine interfaces for robotic VR. *Sci. Adv.* **8**, eabl6700 (2022).
28. Lyu, E. Z. et al. LC repeater-inspired battery-free, chipless, flexible body sensor network with lightweight reader. *IEEE Trans. Instrum. Meas.* **74**, 1–11 (2025).
29. Yan, J. et al. Wireless human motion detection with a highly sensitive wearable pressure sensing technology. *Adv. Mater. Technol.* **8**, 2201936 (2023).
30. Sun, Z. et al. Flexible wireless passive LC pressure sensor with design methodology and cost-effective preparation. *Micromachines* **12**, 976 (2021).
31. Kim, T. et al. 3D designed battery-free wireless origami pressure sensor. *Microsyst. Nanoeng.* **8**, 120 (2022).
32. Yang, C. et al. Ultrathin, lightweight materials enabled wireless data and power transmission in chip-less flexible electronics. *ACS Mater. Au* **5**, 45–56 (2025).
33. Dong, Y. et al. A "two-part" resonance circuit based detachable sweat patch for noninvasive biochemical and biophysical sensing. *Adv. Funct. Mater.* **33**, 2210136 (2023).
34. Liu, F. et al. Self-powered wireless body area network for multi-joint movements monitoring based on contact-separation direct current triboelectric nanogenerators. *InfoMat* **5**, e12428 (2023).
35. Ye, F. et al. Passive wireless body joint-monitoring networks with textile-integrated, strongly coupled magnetic resonators. *Adv. Electron. Mater.* **11**, 2400450 (2025).
36. Wei, Z. et al. Single-fibre-enabled, self-powered wireless body area networks. *Wearable Electron.* **2**, 69–76 (2025).
37. Galli, V. et al. Passive and wireless all-textile wearable sensor system. *Adv. Sci.* **10**, 2206665 (2023).
38. Dautta, M. et al. Programmable multiwavelength radio frequency spectrometry of chemophysical environments through an adaptable network of flexible and environmentally responsive, passive wireless elements. *Small Sci.* **2**, 2200013 (2022).

39. Li, X. et al. Rapid and on-site wireless immunoassay of respiratory virus aerosols via hydrogel-modulated resonators. *Nat. Commun.* **15**, 4035 (2024).
40. Lee, J. et al. Conductive fiber-based ultrasensitive textile pressure sensor for wearable electronics. *Adv. Mater.* **27**, 2433–2439 (2015).
41. Kim, H. et al. In situ formation of Ag nanoparticles for fiber strain sensors: toward textile-based wearable applications. *ACS Appl. Mater. Interfaces* **13**, 39868–39879 (2021).
42. Zhang, Y. et al. High precision epidermal radio frequency antenna via nanofiber network for wireless stretchable multifunction electronics. *Nat. Commun.* **11**, 5629 (2020).
43. Hayati, H. et al. Optimized multi-coil ÿwireless power transfer for experimental neuroscience settings with live animals: a robust design methodology. *Neuroelectronics* **1**, 0003 (2024).
44. Jun, B. O. et al. Miniaturized self-resonant micro coil array with a floating structure for wireless multi-channel transmission. *Adv. Sci.* **8**, 2102944 (2021).
45. Mohan, S. S. et al. Simple accurate expressions for planar spiral inductances. *IEEE J. Solid-State Circuits* **34**, 1419–1424 (1999).
46. Huang, Q. A. et al. LC Passive Wireless Sensors Toward a Wireless Sensing Platform: Status, Prospects, and Challenges. *J. Microelectromech. Syst.* **25**, 822–841 (2016).
47. Munsch, A. E. et al. Quadriceps muscle action and association with knee joint biomechanics in individuals with anterior cruciate ligament reconstruction. *J. Appl Biomech.* **38**, 328–335 (2022).
48. Monte, A. et al. Gastrocnemius Medialis and Vastus Lateralis in vivo muscle-tendon behavior during running at increasing speeds. *Scand. J. Med. Sci. Sports* **30**, 1163–1176 (2020).
49. Xue, B. et al. Limb dominance influences landing mechanics and neuromuscular control during drop vertical jump in patients with ACL reconstruction. *Front Physiol.* **15**, 1488001 (2024).
50. Jibri, Z. et al. Patellar maltracking: an update on the diagnosis and treatment strategies. *Insights Imaging* **10**, 65 (2019).
51. Järvelä, T. et al. Simple measurements in assessing muscle performance after an ACL reconstruction. *Int. J. Sports Med.* **23**, 196–201 (2002).
52. Lee, M. et al. Postoperative long-term monitoring of mechanical characteristics in reconstructed soft tissues using biocompatible, immune-tolerant, and wireless electronic sutures. *ACS Nano* **18**, 12210–12224 (2024).
53. Lee, J. et al. Stretchable and suturable fibre sensors for wireless monitoring of connective tissue strain. *Nat. Electron.* **4**, 291–301 (2021).

Acknowledgements

We thank Professor Sunghoon Lee of the University of Tokyo for his insightful feedback and constructive suggestions. This work was supported by the National Research Foundation of Korea (NRF) grant funded by the Korea government (MSIT) (RS-2021-NR061513, RS-2025-16071089). This research was also supported by Basic Science Research Program through the National Research Foundation of Korea (NRF) funded by the Ministry of Education (RS-2025-25420118). In addition, this work was supported by the Council of Science & Technology (NST) grant by the Korea government (NSIT) (No. GTL25041-000), and the DGIST R&D Program of the Ministry of Science and ICT (2025010373; 25-IRJoint-06).

Author contributions

J.L. conducted the overall experiments, measurements, and analyses and wrote the manuscript. M.L. and H.K. participated in the characterization of the fiber electrode. J.K. designed and fabricated a dip-coating machine for coating the polymer on the scaffold fiber. J.Y. and N.K. performed numerical simulation for the electromagnetic behavior of the textile-based body sensor network. J.L. designed the overall experiment concept, supervised data analysis, supervised the project and contributed to critical revision of the article.

Competing interests

The authors declare no competing interests.

Additional information

Supplementary information The online version contains supplementary material available at https://doi.org/10.1038/s41528-025-00486-5.

Correspondence and requests for materials should be addressed to Jaehong Lee.